ADVANCED MATERIALS
www.advmat.de

Anisotropic Resonant Scattering from Polymer Photonic Crystals

Andrew I. Haines, Chris E. Finlayson, David R. E. Snoswell, Peter Spahn, G. Peter Hellmann, and Jeremy J. Baumberg**

Self-assembly of nanostructures with periodicity on the 100 nm scale produces striking optical effects, including enhanced reflectivity, photonic stop-bands, enhanced optical scattering, and Anderson localization of photons.[1–5] Similar properties have also been widely studied in natural biomaterials which self-assemble in more sophisticated ways, such as butterfly wings, beetle carapaces, and flower petals.[6–8] However, such self-assembly processes intrinsically incorporate disorder in the nanostructures, which degrades the reflectivity but enhances the wider scattering of light. Full understanding of the role of such disorder in optics is currently lacking because the nature of the disorder is not well characterized.

Previous studies of disorder in photonic crystals have demonstrated suppression and broadening of the photonic band gap, and enhancement of diffuse scattering.[9–13] However, analysis of the angle-dependence of scattering has been limited. In high refractive index contrast inverse opals diffuse scattering in band-gap directions is suppressed,[14] but conversely, in the low-contrast regime scattering is enhanced on-resonance.[15] In sedimented opals, polycrystallinity dominates the scattering properties.[16]

Angle-dependent measurements have been limited by current techniques which cannot capture the complete angular range of scattered light. Dark-field spectra give indications of structural order (**Figure 1**a) but do not distinguish the angular (θ) or azimuthal (ϕ) dependence of scattering. Typically, goniometry measurements require very precise alignment, are relatively slow, and are restricted to the plane of incidence. Opaque-screen goniometry allows simultaneous measurement of a range of angles,[17] but so far has been restricted to flat screen geometries limiting its utility to near back-scattering only. We have thus developed a hyperspectral goniometry technique allowing rapid, three-dimensional measurement of optical scattering cones.

Here, we use hyperspectral goniometry on a self-assembling photonic crystal to demonstrate how to completely reconstruct the reciprocal space of scattering vectors. This yields the three-dimensional shape of the dominant reciprocal-lattice point responsible for the intense structural color, and separates resonant and background scattering processes. In these crystals we identify a previously unknown but significant anisotropy of the scattering process which dominates the optical interactions. Such techniques have widespread use in separating the different contributions to disorder and their optical effects.

Collimated light from a supercontinuum laser source is filtered into 10 nm bandwidths by a computer-controlled, liquid crystal tunable filter, and focused to an 80 μm spot on samples mounted on nonreflecting substrates at the center of a translucent white hemispherical screen (Figure 1b). The intensity distribution of scattered light arriving at the thin screen is imaged from the outside with a digital camera. High dynamic range is achieved by combining multiple exposures ranging over three decades.

The flexible single domain photonic-crystal films used are produced by shear ordering of submicrometer-sized hard-core/soft-shell polymer nanospheres.[18–21] These polymer-opal films demonstrate vivid structural color generated by spectrally-resonant Bragg scattering, the saturation of which is strongly enhanced by doping the material with absorptive sub-20-nm carbon nanoparticles.[15,22] The ordering within the material, and consequently the visual iridescence, is greatly improved by an edge-induced rotational shearing process[23] which anneals out disorder to yield close-packed lattices with (111) layers parallel to the film surface.

Because of their low refractive index contrast ($\Delta n \approx 0.1$), light penetrates hundreds of layers into such polymer opals, providing a unique system to study the interplay of order and absorption. In this study, close-packed polymer opals with core sphere radius 85 nm and fill fraction 34% are doped at various levels with carbon nanoparticles (Figure 1b, inset). Following mixing by extrusion, they are rolled into 130 ± 10-μm-thick films and passed through the edge-shearing process several times.[23]

Hyperspectral goniometry measurements yield a composite image at each incident wavelength (**Figure 2**a) which captures the front surface specular reflection peak while clearly resolving the resonant-scattering cone (which is up to two orders of magnitude less intense). The wide angular range collected includes all scattering directions within 90° of the specular reflection at θ_I. Measured intensities are referenced to a standard Lambertian scatterer. The full normalized hyperspectral data set is analyzed with a reciprocal-space transformation[24] which exactly converts the observed angular intensity distribution, $S(\phi, \theta, \lambda)$, into a three-dimensional map of the scattering vectors, $S(\mathbf{q})$.

A. I. Haines, Dr. C. E. Finlayson,
Dr. D. R. E. Snoswell, Prof. J. J. Baumberg
Nanophotonics Centre
University of Cambridge
JJ Thomson Ave, Cambridge, CB3 0HE, UK
E-mail: aih26@cam.ac.uk; jjb12@cam.ac.uk
Dr. P. Spahn, Dr. G. P. Hellmann
Deutsches Kunststoff-Institut (DKI)
Schlossgartenstrasse 6, D-64289 Darmstadt, Germany

DOI: 10.1002/adma.201202169

ADVANCED MATERIALS
www.advmat.de

www.MaterialsViews.com

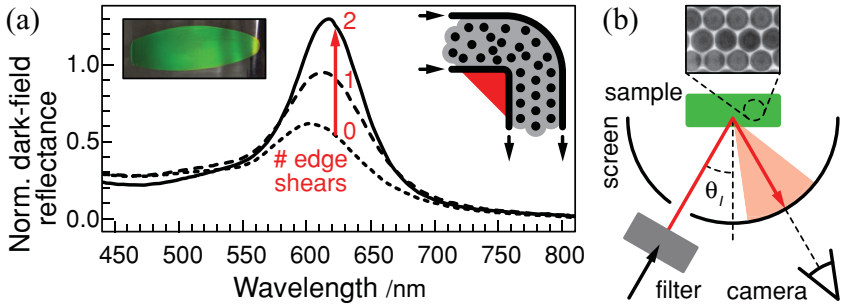

Figure 1. a) Dark-field spectra of polymer-opal films show improving order with edge shearing. Data are normalized to a reference Lambertian scatterer. Inset: (left) photo of polymer-opal film (≈ 6 cm × 2 cm); (right) edge-induced rotational shear processing of core–shell nanospheres between rigid tapes. b) Experimental setup. Collimated white laser light passes through tunable-wavelength filter; monochromatic light striking sample at angle θ_I is reflected (arrow) and scattered (cone) onto hemispherical screen and externally imaged. Inset: transmission electron micrograph of the (111) layer in polymer opal (0.8 μm × 0.6 μm) showing the 170 nm diameter spherical cores.[18]

With the sample in the xy plane and light incident in the xz plane at an angle θ_I to the z axis, the change in wavevector for scattering into the direction with spherical polar angles (ϕ, θ) is $\mathbf{q} = \tilde{k}_0 (\cos\varphi \sin\tilde{\theta} - \sin\tilde{\theta}_I, \sin\varphi \sin\tilde{\theta}, \cos\tilde{\theta} + \cos\tilde{\theta}_I)$, where tildes denote quantities measured inside the sample and $\tilde{k}_0 = 2\pi/\tilde{\lambda}$. The internally and externally measured values are related by the average refractive index, $\bar{n}$: $\tilde{\lambda} = \lambda/\bar{n}$, $\sin\tilde{\theta} = \sin\theta/\bar{n}$. Samples are mounted so that processing (rolling and subsequent edge-shearing) was aligned in the x direction. The camera is directed along the specular reflection rather than the sample normal and the coordinates subsequently rotated into the correct reciprocal-space orientation.[24]

By measuring in spectral slices from 450–700 nm at an incidence angle of 30°, we thus reconstruct the full scattering distribution $S(\mathbf{q})$. This reveals strong scattering around the (111) reciprocal-lattice point, $\mathbf{g}_{111} = (0, 0, 31\ \mu m^{-1})$, for these polymer opals (Figure 2b). It is immediately clear that the scattering is anisotropic in all three directions, appearing as a flattened ellipsoid. While we have previously reported an anisotropic response to stress,[25] the optical anisotropy presented here is intrinsic to the nanostructure, appearing in all unstretched samples.

To closely examine the nonspecular scattering, the intense front surface reflection is removed. We fit the resulting reciprocal-lattice scattering distribution around $\mathbf{g}_{111}$ with a three-dimensional Gaussian function to find the amplitude and wavevector widths, $\Gamma_{x,y,z}$. The overall scattering strength, $S_{111} = \int S(\mathbf{q})\ d^3\mathbf{q}$ (integrated over the full reciprocal-lattice spot), is greatly enhanced by the edge-shear process, linearly increasing by 300% over two passes (**Figure 3**a,b). The shape of the reconstructed reciprocal-lattice spot reveals both disorder in the average layer spacing (q_z) as well as in-plane defects ($q_{x,y}$). In every case we find strongly anisotropic scattering, with $\Gamma_y > \Gamma_x > \Gamma_z$ (Figure 3c).

The average variation in layer spacing, $\Gamma_z/g_{111} \approx \pm 3\%$, corresponds to the displacement required for individual spheres to squeeze through the gap between neighboring spheres in the layer above or below. Edge-shearing causes a slow decrease in this disorder (Figure 3d), but the continued movement of spheres throughout annealing keeps the layers apart and thus some variation in spacing remains.

The measured in-plane scattering $S(q_x, q_y)$ clearly shows anisotropic disorder in each sheet layer with $\Gamma_y \approx 2\Gamma_x$. The Fourier relation to real space indicates the size scale of the defects and suggests that additional sphere chains aligned along x are responsible. We test this hypothesis, modeling such defects by inserting a short chain into a hexagonally-close-packed layer of spheres and relaxing the resulting forces (**Figure 4**a). Direct calculation of the resulting scattering vectors $S(\mathbf{q})$[26] produces anisotropic scattering in agreement with that observed in our samples (Figure 4b). The average size of the defects in our samples (estimated from $g_{111}/\Gamma_{x,y}$) is 5 spheres wide and 10 spheres long, with an approximately Gaussian shape. Our results show that edge-shearing does not anneal these defects out, and they may even lead to the degradation of order on further shearing passes. The 40° angular range of the scattering cone which controls the structural color in such systems is thus entirely set by these chain defects, whose origin is not yet understood microscopically.

Because the shape of the reciprocal space spot is unaffected by edge-shearing, the observed increase in scattering strength (S_{111}) upon shearing must be caused by an increase in either the effective number of ordered layers or the effective refractive index contrast. However, cross-sections show that samples are ordered throughout their thickness,[23] eliminating the former mechanism. The latter is determined by the intrinsic refractive index contrast between the shell and core polymers, Δn, but is also affected by the degree to which spheres are vertically displaced about the mean layer spacing.

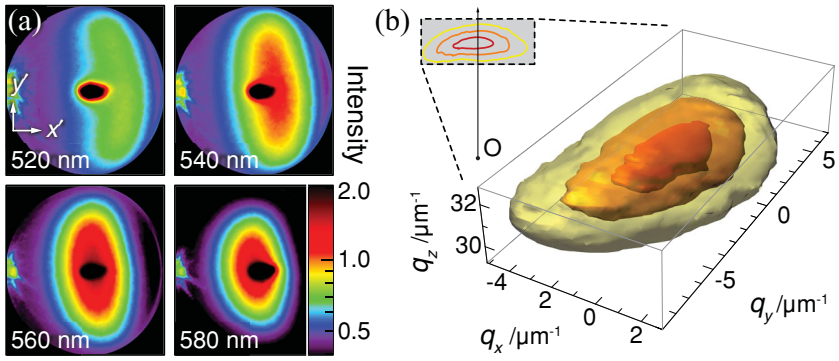

Figure 2. a) High dynamic range false color images of scattering from polymer opal at various wavelengths collected on a hemispherical screen, showing highly anisotropic scattering. The small black spot in the center is the intense specular reflection; the hole through which light is introduced is seen on the left. b) Three-dimensional contour plot of reconstructed reciprocal-space scattering distribution at (from innermost contour outwards) 180, 140, and 100% of a reference Lambertian scatterer. Inset: scattering slice $S(0, q_y, q_z)$.

Adv. Mater. **2012**,
DOI: 10.1002/adma.201202169

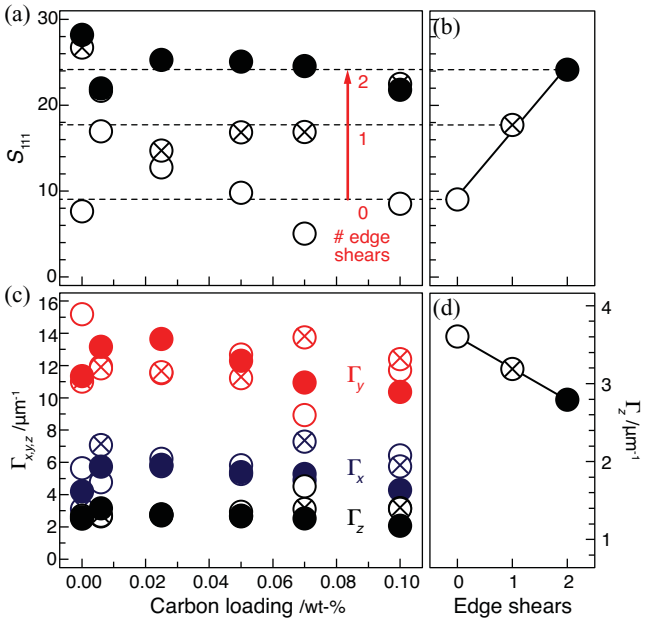

Figure 3. a,b) Integrated scattering intensity (S_{111}) shows (a) little dependence on carbon loading (random variations due to variability of sample preprocessing) and (b) linear increase with edge shearing passes (empty, crossed, and filled circles denote 0, 1, and 2 passes, respectively). c) Full-widths at half maximum ($\Gamma_{x,y,z}$) of Gaussian fits to reciprocal-space scattering distributions. The smallest disorder is in the average layer spacing (Γ_z, black). In-layer disorder is greater in the *y* direction (Γ_y, red) than in the processing direction (Γ_x, blue). d) Disorder in average layer spacing, Γ_z, decreases linearly with edge shearing.

To determine how this kind of disorder can affect the effective refractive index contrast, we model the material as a close-packed lattice of high-index spheres embedded in a continuous matrix of low-index shell (Figure 4c). The fill fraction sets the radius of the spheres, *r*, to be up to half the lattice constant. Allowing for layer spacings, *L*, which can vary around the close-packed separation and given random displacements, $\delta_{1,2}$, of spheres from the upper and lower layers of a unit cell, we calculate the effective refractive index profile at a depth *z*,

$$\bar{n}(z, \delta_1, \delta_2) = n_{\text{shell}} + \Delta n\, f(z, \delta_1, \delta_2)$$

where $f(z, \delta_1, \delta_2) = \pi\left(r_1^2 + r_2^2\right)/2\sqrt{3}$ is the fill fraction per unit area, with $r^2{}_1 = r^2 - (z - \delta_1)^2$, $r^2{}_2 = r^2 - (L - z + \delta_2)^2$. The effective refractive index profile is obtained by averaging over all possible random displacements,

$$\bar{n}(z) = n_{\text{shell}} + \Delta n \int f(z, \delta_1, \delta_2)\, D(\delta_1)\, D(\delta_2)\, \mathrm{d}\delta_1\, \mathrm{d}\delta_2$$

and employing a normal distribution with zero mean and standard deviation σ for the disorder distribution *D*. The effective refractive index contrast, $\Delta\bar{n}$,[27] decreases as disorder increases (Figure 4d), due to the layers becoming increasingly blurred. Optimum contrast is achieved at $r = 0.41$, corresponding to a volume fill fraction of 41%.

The chain defects and layer disorder, which set the widths of the scattering cone and thus determine the perceived color properties, are little modified by the presence of the carbon nanoparticles. The effect of the latter is instead predominantly on the large-angle scattering background, produced by multiple scattering inside the sample.[28] Averaging this background outside the $\mathbf{g}_{111}$ spot shows its suppression as carbon doping increases (**Figure 5**a). To compare with the absorption length, we measure transmission through equivalent polymer-opal films in which the refractive index contrast has been chemically balanced ($\Delta n = 0$).[29]

We model the background-generating multiple scattering using a Monte Carlo simulation of propagation in a semi-infinite homogenous scattering medium with exponentially distributed free paths of mean length ℓ. The background scattering intensity for absorption length α is then given by

$$I(\alpha) = \int_0^\infty e^{-z/\alpha} L(z)\, \mathrm{d}z$$

where *L* is the backscatter path-length distribution. A good fit to our data plotted against α (Figure 5b) is achieved with a mean free path of 820 nm and an angular scattering distribution dominated by forward scattering of width ±38° (Figure 5b, inset), giving a mean backscatter path length of 76 μm, similar to that measured previously.[22] Most scattering paths are shorter than the absorption length, so that only the rare longer paths are strongly attenuated. Consequently, while the absorption length drops by a factor of 16 over the range of carbon dopings used in this study, the background scatter is only halved. The origin of background scattering is thus completely separate to the resonant scattering in such nanostructures; it arises from local shape or size polydispersity, but is totally unaffected by global ordering. This strategy to enhance color saturation resembles that in many biophotonic structures which incorporate pigments, but here is quantitatively explained.

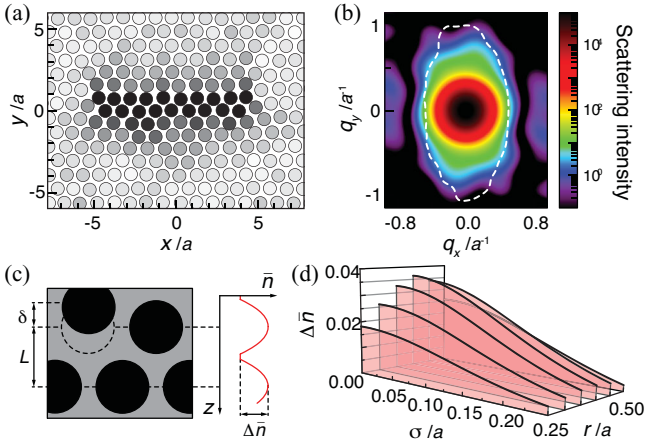

Figure 4. a) Simulated ten-sphere chain defect shaded according to displacement from a perfect hexagonal lattice of spacing *a*, with darker spheres being further from lattice points. b) Calculated scattering intensity[26] of ten-sphere chain defect with 125% contour of experimental $S(\mathbf{q})$ from Figure 2b (dashed). c) Side view of close-packed lattice showing two layers of high-index cores (black) surrounded by low-index shell matrix (grey). One sphere is displaced from the layer by δ; these random displacements throughout layers decrease the effective refractive index contrast. d) Effective refractive index contrast ($\Delta\bar{n}$) shows decrease with disorder (σ) and an optimal particle size (*r*).

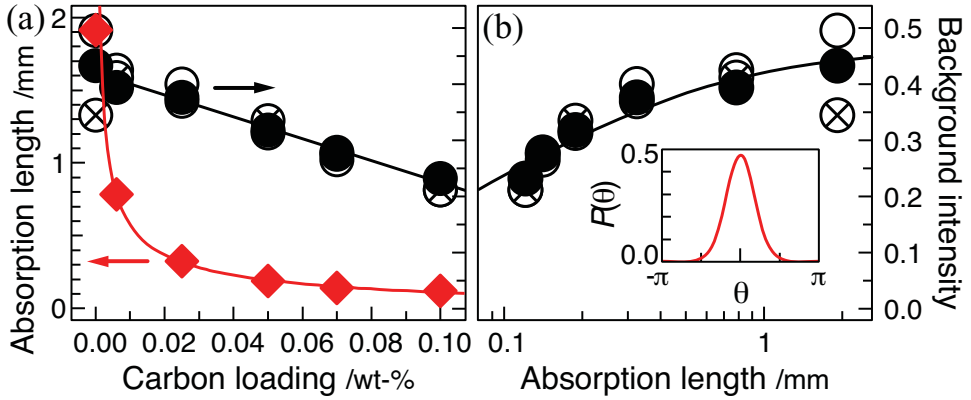

Figure 5. a) Normalized average background scattering intensity (black, right axis) decreases linearly while absorption length in index-matched polymer opals (red, left axis) drops exponentially with carbon loading. b) Calculated background scattering intensity from Monte Carlo simulation (line) using a mean free path of 820 nm fits well the measured intensities (points). Inset: probability density function of best-fit Mie scattering angle distribution used in simulation shows forward dominated scattering.

In summary, these results show how proper reconstruction of the scattering vectors from a nanostructure using hyperspectral goniometry gives detailed insights into their structural color properties. In our polymer opals this reveals the strongly anisotropic nature of the resonant scattering process. The increase in scattering strength with shear processing is shown to arise from the increasing effective refractive index contrast with improving order. We find that chain defects govern the observed angular scattering cone which sets the strongly colored appearance, and their control is thus crucial in self-assembly. Absorptive doping eliminates the multiply scattered background without affecting the resonant scattering. Such full measurements of the scattering are thus crucial to understand optical scattering in nanostructures and underpin novel biomimetic strategies.

Supporting Information

Supporting Information is available from the Wiley Online Library or from the author.

Received: May 30, 2012
Revised: July 11, 2012
Published online:

[1] J. E. G. J. Wijnhoven, W. L. Vos, *Science* **1998**, *281*, 802–804.
[2] Y. A. Vlasov, X.-Z. Bo, J. C. Sturm, D. J. Norris, *Nature* **2001**, *414*, 289–293.
[3] A. F. Koenderink, M. Megens, G. van Soest, W. L. Vos, A. Lagendijk, *Phys. Lett. A* **2000**, *268*, 104–111.
[4] S. John, *Phys. Rev. Lett.* **1987**, *58*, 2486–2489.
[5] D. S. Wiersma, P. Bartolini, A. Lagendijk, R. Righini, *Nature* **1997**, *390*, 671–673.
[6] P. Vukusic, J. R. Sambles, *Nature* **2003**, *424*, 852–855.
[7] A. R. Parker, V. L. Welch, D. Driver, N. Martini, *Nature* **2003**, *426*, 786–787.
[8] H. M. Whitney, M. Kolle, P. Andrew, L. Chittka, U. Steiner, B. J. Glover, *Science* **2009**, *323*, 130–133.
[9] Y. A. Vlasov, V. N. Astratov, A. V. Baryshev, A. A. Kaplyanskii, O. Z. Karimov, M. F. Limonov, *Phys. Rev. E* **2000**, *61*, 5784–5793.
[10] R. Rengarajan, D. Mittleman, C. Rich, V. Colvin, *Phys. Rev. E* **2005**, *71*, 0166115.
[11] J. F. Galisteo-López, M. Galli, M. Patrini, A. Balestreri, L. C. Andreani, C. López, *Phys. Rev. B* **2006**, 125103.
[12] P. D. García, R. Sapienza, L. S. Froufe-Pérez, C. López, *Phys. Rev. B* **2009**, *79*, 241109.
[13] P. D. García, R. Sapienza, C. Toninelli, C. López, D. S. Wiersma, *Phys. Rev. A* **2011**, *84*, 023813.
[14] A. F. Koenderink, W. L. Vos, *J. Opt. Soc. Am. B* **2005**, *22*, 1075–1084.
[15] O. L. J. Pursiainen, J. J. Baumberg, H. Winkler, B. Viel, P. Spahn, T. Ruhl, *Opt. Express* **2007**, *15*, 9553–9561.
[16] V. N. Astratov, S. Fricker, M. S. Skolnick, D. M. Whittaker, P. N. Pusey, A. M. Adawi, *Phys. Rev. B* **2002**, *66*, 165215.
[17] A. V. Baryshev, A. A. Kaplyanskii, V. A. Kosobukin, K. B. Samusev, D. E. Usvyat, M. F. Limonov, *Phys. Rev. B* **2004**, *70*, 11304.
[18] T. Ruhl, P. Spahn, G. P. Hellmann, *Polymer* **2003**, *44*, 7625–7634.
[19] T. Ruhl, P. Spahn, H. Winkler, G. P. Hellmann, *Macromol. Chem. Phys.* **2004**, *205*, 1385–1393.
[20] O. L. J. Pursiainen, J. J. Baumberg, H. Winkler, B. Viel, P. Spahn, T. Ruhl, *Adv. Mater.* **2008**, *20*, 1484–1487.
[21] D. R. E. Snoswell, A. Kontogeorgos, J. J. Baumberg, T. D. Lord, M. R. Mackley, P. Spahn, G. P. Hellmann, *Phys. Rev. E* **2010**, *81*, 020401.
[22] J. J. Baumberg, O. L. J. Pursiainen, P. Spahn, *Phys. Rev. B* **2009**, *80*, 201103.
[23] C. E. Finlayson, P. Spahn, D. R. E. Snoswell, G. Yates, A. Kontogeorgos, A. I. Haines, G. P. Hellmann, J. J. Baumberg, *Adv. Mater.* **2011**, *23*, 1540–1544.
[24] See the Supporting Information for full details of the reciprocal-space transformation, including the rotation from camera- to sample-oriented coordinates.
[25] A. Kontogeorgos, D. R. E. Snoswell, C. E. Finlayson, J. J. Baumberg, P. Spahn, G. P. Hellmann, *Phys. Rev. Lett.* **2010**, *105*, 233909.
[26] In-plane scattering from the two-dimensional lattice (Figure 4a) is approximated by Fourier transforming, neglecting the form factor.
[27] The effective refractive index contrast is given by the first component of the discrete cosine transform of the depth-dependent refractive index.
[28] J. D. Forster, H. Noh, S. F. Liew, V. Saranthan, C. F. Schreck, L. Yang, J.-G. Park, R. O. Prum, S. G. J. Mochrie, C. S. O'Hern, H. Cao, E. R. Dufresne, *Adv. Mater.* **2010**, *22*, 2939–2944.
[29] C. E. Finlayson, A. I. Haines, D. R. E. Snoswell, A. Kontogeorgos, J. J. Baumberg, P. Spahn, G. P. Hellmann, *Appl. Phys. Lett.* **2011**, *99*, 261913.

DOI: 10.1002/adma.201202169